Robust Identification of Object Elasticity

Huafeng $\mathrm{Liu}^{1,2}$ and Pengcheng Shi^2

State Key Laboratory of Modern Optical Instrumentation
 Zhejiang University, Hangzhou, China

 Department of Electrical and Electronic Engineering

Hong Kong University of Science and Technology, Hong Kong

Abstract. Quantification of object elasticity properties has important technical implications as well as significant practical applications, such as civil structural integrity inspection, machine fatigue assessment, and medical disease diagnosis. In general, given noisy measurements on the kinematic states of the objects from imaging or other data, the aim is to recover the elasticity parameters for assumed material constitutive models of the objects. Various versions of the least-square (LS) methods have been widely used in practice, which, however, do not perform well under reasonably realistic levels of disturbances. Another popular strategy, based on the extended Kalman filter (EKF), is also far from optimal and subject to divergence if either the initializations are poor or the noises are not Gaussian. In this paper, we propose a robust system identification paradigm for the quantitative analysis of object elasticity. It is derived and extended from the \mathcal{H}_{∞} filtering principles and is particularly powerful for real-world situations where the types and levels of the disturbances are unknown. Specifically, we show the results of applying this strategy to synthetic data for accuracy assessment and for comparison to LS and EKF results, and using canine magnetic resonance imaging data for the recovery of myocardial material parameters³.

1 Introduction

Quantitative and noninvasive assessment of the intrinsic material properties provides invaluable insights into the objects' physical conditions, i.e. the structural integrity of bridges and the material fatigue states of airplanes. Of particular current interests, there have been plenty studies on living soft tissues, such as heart [2,9], breast [5,10], skin [11], and blood vessels [8], under the clinical assumptions that diseases are highly correlated with changes of local tissue elasticity. From computer vision and medical image analysis perspectives, the goal is to use image-derived noisy observations on the kinematic states to arrive at accurate, robust, and meaningful measurement of the object elasticity distribution, where the recovered information is key to the better formulation and understanding of many physically-based vision problems, including motion tracking, object segmentation, virtual-reality systems, and computer-assisted diagnosis.

³ This work is supported in part by Hong Kong Research Grant Council under CERG project HKUST6151/03E and by the National Basic Research Program of China (No: 2003CB716104).

M. Šonka et al. (Eds.): CVAMIA-MMBIA 2004, LNCS 3117, pp. 423-435, 2004.

[©] Springer-Verlag Berlin Heidelberg 2004

1.1 Related Works

The forward processes, which provide the image-derived measurement data on the kinematic states, have strong implications on the reliability of the inverse processes, which recover the material parameters. In addition to reservoir of motion analysis strategies in computer vision, there have been efforts aimed at establishing displacement fields from specialized medical imaging techniques, such as elastography [6] which measures tissue motion induced by external or internal forces, and magnetic resonance (MR) tagging [14] which creates a sparse magnetization grid that tags the underlying tissue and provides tissue movement information through the tracking of the grid deformation.

The inverse algorithms, which are the main focuses of this paper, reconstruct the elasticity distributions from the motion measurement data. The first type of efforts attempt to quantify the material Young's modulus by inverting the measured mechanical responses based on numerical solution of the elasticity equation [4], which describes the mechanical equilibrium of a deformed medium. Ignoring terms related to pressure, the equation becomes a function of the spatial derivatives of the Young's modulus E, which, in principle, could then be used to reconstruct the distribution of E [10]. An related approach re-arranges the linearly discretized equations that describe the forward problem, such that the modulus distribution directly becomes the unknown variables to be solved [7].

The second group of efforts try to minimize criteria that measure the goodness of fit between the model-predicted and data-measured mechanical responses. In [2], finite element (FE) meshes are constructed with loading parameters measured during imaging. FE solutions are then performed using small-strain, small-displacement theory, and corresponding strains are computed independently using imaging-derived data. The material parameters are determined for strain energy functions that maximize the agreement between the observed (from imaging) and the predicted (from FE analysis) strains. Similar in spirit, iterative descent methods are used for various FE models of the elasticity equations to fit, in least-squares sense, a set of tissue displacement fields [5,11].

1.2 Contributions

We present several robust estimation schemes for the recovery of object elasticity parameters from imaging data. Constructing the object dynamics from continuum mechanics laws and finite element method, we convert the system equation into state-space representation, which is further reformulated as a general non-linear system identification problem for the spatially varying material Young's modulus. Within this paradigm, we examine the validity and limitations of the existing works, largely based on the least-square (LS) estimators and the extended Kalman filters (EKF), both of which adopt the minimum-mean-square-error criteria in terms of the reconstructed state, and assume that the noises of the measurement data are Gaussian. We then present two robust strategies, the full-state-derivative information (FSDI) and the noise-perturbed full-state information (NPFSI) methods, which are derived and extended from

the \mathcal{H}_{∞} filtering principles and provide the minimum-maximum-error (minimax) solutions to the material property estimation problem, without assumptions on the noise statistics. Using synthetic data, we investigate the sensitivity of the algorithms towards noise types and levels, as well as towards system initializations. The experimental results show consistently superior performance of the robust methods, especially the NPFSI form, over the LS and EKF algorithms for non-Gaussian data. We also present EKF and NPFSI estimation results from MR imaging data of a canine heart, both showing good agreement with histological tissue staining of the myocardium, the clinical gold standard.

2 Parameter Identification Problem Formulation

2.1 Continuum Mechanics Model and State-Space Representation

In general, natural objects such as biological tissues have very complicated continuum mechanical properties in terms of their constitutive laws [4]. For computational simplicity and feasibility, we assume that the objects under consideration are nearly incompressible linear elastic solids. For such a material, the strain energy function \mathcal{W} has the form $\mathcal{W} = \frac{1}{2}c_{ijkl}\varepsilon_{ij}\varepsilon_{kl}$, where ε_{ij} and ε_{kl} are components of the infinitesimal strain tensor and c_{ijkl} is the material specific elastic constant. In our case, the stress-strain relationship obeys the Hooke's law, which states that the stress tensor σ_{ij} is linearly proportional to the stain tensor: $\sigma_{ij} = c_{ijkl}\varepsilon_{kl}$. Under the assumptions that the material is isotropic, where the elastic properties are identical in all directions, and the strain and stress tensors are symmetric, there are exactly two elastic constants which characterize the material and we have the linear isotropic constitutive relationship:

$$\sigma_{ij} = \lambda \delta_{ij} \varepsilon_{kk} + 2\mu \varepsilon_{ij} \tag{1}$$

where λ and μ are the *Lame* constants, and δ_{ij} is the Kronecher's delta function. In matrix form, under two dimensional Cartesian coordinate system, $[\sigma] = [D][\varepsilon]$. Assuming the displacement components along the x- and y-axis to be u(x,y) and v(x,y) respectively, the infinitesimal strain tensor $[\varepsilon]$ and the material matrix [D] under plane strain situation are:

$$[\varepsilon] = \begin{bmatrix} \frac{\partial u}{\partial x} \\ \frac{\partial v}{\partial y} \\ \frac{\partial u}{\partial y} + \frac{\partial v}{\partial x} \end{bmatrix} = \begin{bmatrix} \frac{\partial}{\partial x} & 0 \\ 0 & \frac{\partial}{\partial y} \\ \frac{\partial}{\partial y} & \frac{\partial}{\partial x} \end{bmatrix} \begin{bmatrix} u \\ v \end{bmatrix}$$

$$[D] = E \begin{bmatrix} \frac{1-\nu}{(1+\nu)(1-2\nu)} & \frac{\nu}{(1+\nu)(1-2\nu)} & 0 \\ \frac{\nu}{(1+\nu)(1-2\nu)} & \frac{1-\nu}{(1+\nu)(1-2\nu)} & 0 \\ 0 & 0 & \frac{1-2\nu}{2(1+\nu)(1-2\nu)} \end{bmatrix}$$
(2)

Here, derived from the *Lame* constants, the Young's modulus E measures of the stiffness and the Poisson's ratio ν measures the compressibility of the material.

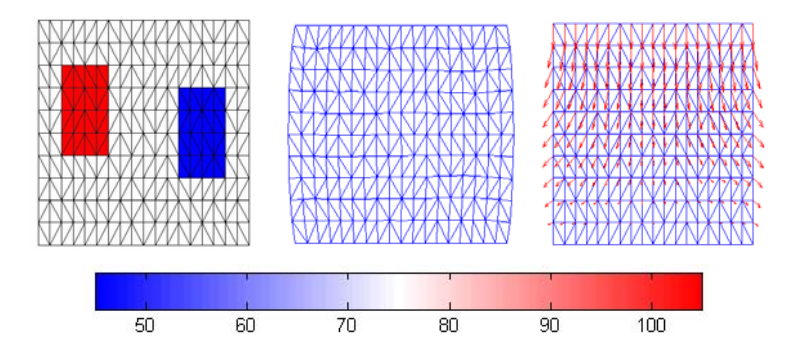


Fig. 1. Generation of the synthetic kinematic data: original state (left), deformed state (middle), and the displacement field (right). The colors of the left figure indicate the Young's moduli of the hard (red), normal (white), and soft (blue) tissues, respectively.

The finite element method is used to discretize the regions of interests into small elements, the Delaunay triangles of the sampling nodes in our implementation. Specifically, an isoparametric formulation defined in a natural coordinate system is used, in which the interpolation of the element coordinates and element displacements use the same basis functions. The nodal displacement based governing dynamic equation of each element is established under the minimum potential energy principle [1], and is then assembled together in matrix form as

$$M\ddot{U} + C\dot{U} + KU = R \tag{3}$$

with mass matrix M, stiffness matrix K which is related to the material Young's modulus E and Poisson's ratio ν , and Rayleigh damping matrix $C = \alpha M + \beta K$.

Equation 3 can be converted into a state-space representation of a continuous time linear system by making $x = (U, \dot{U})^T$ (T denotes transpose) such that:

$$\dot{x}(t) = A(\theta)x(t) + Bw(t) \tag{4}$$

where the material parameter vector θ , the state vector x, the system matrices A and B, and the control (input) term w are:

$$\theta = E \quad x(t) = \begin{bmatrix} U(t) \\ \dot{U}(t) \end{bmatrix}, \quad w(t) = \begin{bmatrix} 0 \\ R \end{bmatrix},$$
$$A = \begin{bmatrix} 0 & I \\ -M^{-1}K & -M^{-1}C \end{bmatrix}, \quad B = \begin{bmatrix} 0 & 0 \\ 0 & M^{-1} \end{bmatrix}$$

Note that, for this particular paper, we are only interested in estimating the Young's modulus whereas the Poisson's ratio is fixed. In principle, however, both E and ν can be estimated simultaneously [9].

2.2 System Dynamics in Parameter Identification Form

Since our goal is to recover the parameter vector $\theta = E$, instead of the more typical problem of estimating the state vector x, the system Equation 4 needs to be reformulated in the form of $\dot{x}(t) = \mathcal{A}_c(x(t))\theta + \mathcal{B}_c$ to facilitate the process. Submitting in $C = \alpha M + \beta K$ and rearranging the system equation to:

$$\begin{bmatrix} \dot{U}(t) \\ \ddot{U}(t) \end{bmatrix} = \begin{bmatrix} 0 & \dot{U} \\ -M^{-1}KU & -\alpha\dot{U} - \beta M^{-1}K\dot{U} \end{bmatrix} + \begin{bmatrix} 0 & 0 \\ 0 & M^{-1} \end{bmatrix} \begin{bmatrix} 0 \\ R \end{bmatrix}$$
 (5)

we now need to convert all the terms which contain K into functions of E: $KU = G_1E$ and $K\dot{U} = G_2E$.

According to the finite element method, the global stiffness matrix K is assembled from the element stiffness K_e :

$$K = \sum K_e = \sum \int_{\Omega_e} B_e^T D_e B_e \ d\Omega_e \tag{6}$$

where Ω_e is the domain of an arbitrary element e, B_e is the local element straindisplacement matrix, and D_e is the element material matrix. The element stiffness matrix K_e can then be stated in terms of its unknown Young's modulus E_e :

$$K_e = E_e \int_{\Omega_e} B_e^T D_e' B_e \ d\Omega_e = E_e K_e' \tag{7}$$

Then, the iterative steps of recasting KU to G_1E (and $K\dot{U}$ to G_2E in the exactly same fashion) are:

- 1. Initialize a $N \times N_e$ null matrix G_1 with zero entries, where N = number of system nodal variables and $N_e =$ number of system elements.
- 2. Initialize a $N \times N$ null matrix K_s with zero entries.
- 3. For an arbitrary element N_x , construct the local element matrix K'_{N_x} following Equation 7.
- 4. Using established correspondence between local and global numbering schemes, change the subscript indices of the coefficients in the K'_{N_x} matrix to the global indices.
- 5. Insert K'_{N_x} terms into the corresponding K_s matrix in the locations designated by their indices.
- 6. Insert K_sU , which is now a column vector reflecting the contribution by element N_x , to the N_x^{th} column of the G_1 matrix.
- 7. Return to step 2 and repeat this procedure for next element until all elements have been so treated.

Once the numerical procedures of computing G_1 and G_2 are completed, Equation 5 is converted into the parameter identification form which can be used for the estimation of the Young's modulus distribution:

$$\dot{x}(t) = Fx + \mathcal{A}_c(x(t))\theta + B_c w(t) \tag{8}$$

Table 1. Estimated Young's moduli from the synthetic data. Each data cell represents the mean \pm standard derivation for the normal (75), hard (105), and soft (45) tissues

Method	Tissue	Noise-Free	20dB(Gau)	30dB(Gau)	20dB(Poi)	30dB(Poi)
LS	Normal	75.0 ± 0.0	FAILED	74.9 ± 2.9	FAILED	75.1 ± 3.6
	Hard	105.0 ± 0.0	FAILED	106.2 ± 9.1	FAILED	104.8 ± 7.9
	Soft	45.0 ± 0.0	FAILED	45.3 ± 3.2	FAILED	44.9 ± 2.8
EKF	Normal	74.9 ± 1.7	76.0 ± 5.5	76.6 ± 3.0	77.1 ± 6.6	75.0 ± 3.6
	Hard	105.2 ± 1.0	$101.8 \!\pm 10.1$	104.2 ± 3.8	100.6 ± 23.0	103.8 ± 9.9
	Soft	46.0 ± 1.8	46.0 ± 3.8	47.1 ± 3.4	50.1 ± 5.7	47.9 ± 3.8
FDSI	Normal	75.0 ± 0.0	FAILED	74.8 ± 5.0	FAILED	75.1 ± 3.0
	Hard	105.0 ± 0.0	FAILED	106.4 ± 9.4	FAILED	104.7 ± 5.8
	Soft	45.0 ± 0.0	FAILED	45.4 ± 5.7	FAILED	44.9 ± 1.3
NPFSI	Normal	74.8 ± 1.5	73.3 ± 8.4	73.8 ± 3.4	74.8 ± 7.2	73.9 ± 3.1
	Hard	104.1 ± 1.2	100.9 ± 24.0	102.6 ± 9.1	100.1 ± 15.7	102.3 ± 7.2
	Soft	46.3 ± 2.1	47.0 ± 5.9	44.9 ± 2.7	45.2 ± 4.6	44.8 ± 2.5

where

$$\theta = E, \quad x(t) = \begin{bmatrix} U(t) \\ \dot{U}(t) \end{bmatrix}, \quad w(t) = \begin{bmatrix} 0 \\ R \end{bmatrix},$$

$$\mathcal{A}_c = \begin{bmatrix} 0 & 0 \\ -M^{-1}G_1 & -\beta M^{-1}G_2 \end{bmatrix}, \quad B_c = \begin{bmatrix} 0 & 0 \\ 0 & M^{-1} \end{bmatrix}, \quad F = \begin{bmatrix} 0 & I \\ 0 & -\alpha I \end{bmatrix}$$

3 Parameter Identification Algorithms

3.1 Synthetic Data for Evaluation

In order to illustrate the accuracy and robustness of the material parameters estimates, synthetic data with known kinematics are generated, as shown in Fig. 1. The rectangular testing object, with dimension of 28 (height) x 16 (width) x 1 (thickness), is made of three components of different material elasticities, $E_{hard}=105$ for the hard (red) part, $E_{normal}=75$ for the normal (white) part, and $E_{soft}=45$ for the soft (blue) part, while Poisson's ratio is set to 0.49 for all parts. The elastic medium is constrained to deform 1.2 displacement in the vertical direction at the top side and 0 at the bottom side. Using these boundary conditions, we solve the forward problem and the resulting displacements are labelled as the ideal measurement data. Different types and levels of noises are then added to generate the noisy data.

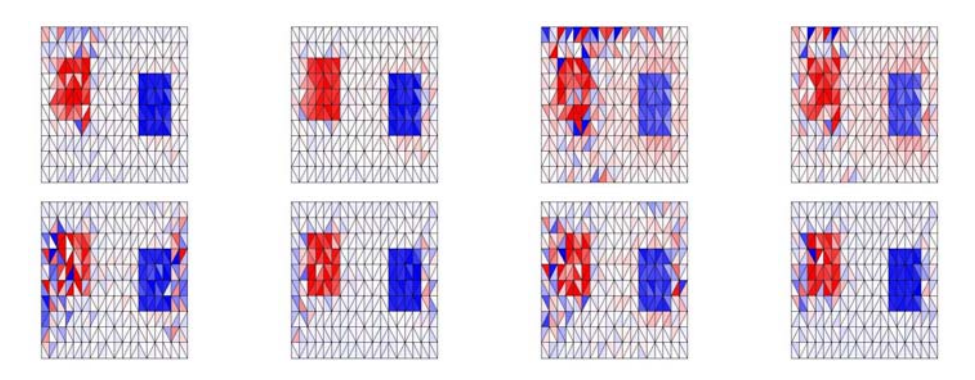


Fig. 2. Estimated elasticity modulus distributions using the EKF (top row) and NPFSI (bottom row) methods for noisy input data (left to right): SNR = 20dB (Gaussian), SNR = 30dB (Gaussian), SNR = 20dB (Poisson), and SNR = 30dB (Poisson).

3.2 Least Squares Approximation

Least-squares algorithms are often considered static, where the uncertainties of the measurements and the system are not of concern. Rearrange Equation 8 as:

$$\mathcal{A}_c(x)\theta = \dot{x} - Fx - B_c w(t) = \dot{x} - \mathcal{B} \tag{9}$$

the parameter vector θ can then be directly estimated from the least-squares approximation:

$$\hat{\theta} = [\mathcal{A}_c^T \mathcal{A}_c]^{-1} \mathcal{A}_c^T (\dot{x} - \mathcal{B}) \tag{10}$$

Method Evaluation Using the synthetic data, the LS estimated Young's modulus values for ideal and noisy inputs of displacement measurements are shown in Table 1. For clean and low noise (30dB) cases, the LS method does give excellent performance. However, when the noise levels (20dB) increase, LS fails to provide any meaningful results. Clearly, the LS strategy does not have the capability to handle uncertainties of the system modeling and the measurement data. Further, it is actually a pseudo-inverse process, and we are going to discuss the more efficient least-square solution based on the Kalman filters.

3.3 Extended Kalman Filter

The EKF approach to parameter estimation in dynamical system has a rather long history. It has the flexibility to easily incorporate both system modeling and measurement uncertainties. The basic idea is to consider system parameters as part of an augmented state vector, and with measurements taken over time, the

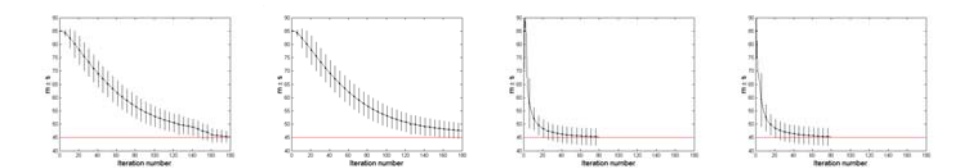


Fig. 3. Converging speed of the average Young's modulus in the soft region using EKF (the two left figures) and $\mathcal{H}_{\infty}(NPFSI)$ (the two right figures) methods: SNR = 30dB Gaussian inputs and SNR = 30dB Poisson inputs

system response and the parameter estimates are adjusted so that they match the data in an optimal manner:

$$\begin{bmatrix} \dot{x(t)} \\ \dot{\theta} \end{bmatrix} = \begin{bmatrix} Fx + \mathcal{A}_c(x)\theta + B_cw(t) \\ 0 \end{bmatrix} + \begin{bmatrix} v(t) \\ 0 \end{bmatrix}$$
 (11)

$$y = \begin{bmatrix} I \ 0 \end{bmatrix} \begin{bmatrix} x \\ \theta \end{bmatrix} + e(t) \tag{12}$$

This augmented system is nonlinear due to the cross-product between x and θ . If the process noise v(t) and measurement noise e(t) are both white Gaussian with covariances Q_v and R_e respectively, the EKF solution comes from [12]:

$$\begin{bmatrix} \dot{x}(t) \\ \dot{\hat{\theta}} \end{bmatrix} = \begin{bmatrix} F\hat{x} + \mathcal{A}_c(\hat{x})\hat{\theta} + B_c w(t) \\ 0 \end{bmatrix} + PH^T R_e(t)^{-1} [y - H\hat{z}]$$
 (13)

$$\dot{P} = LP + PL^{T} + Q_{v} - PH^{T}R_{e}(t)^{-1}HP$$
(14)

where
$$P(0) = P_0 > 0$$
, $H = \begin{bmatrix} I & 0 \end{bmatrix}$, and $L = \begin{bmatrix} F + \frac{\partial}{\partial \hat{x}} \{ \mathcal{A}_c(x) \hat{\theta} + B_c w(t) \} & \mathcal{A}_c(\hat{x}) \\ 0 & 0 \end{bmatrix}$.

One difficulty EKF faces is that there is no general, cost effective theory for choosing optimal R_e , Q_v and P_0 . Prior knowledge thus often plays important roles in the *ad hoc* determination of these parameters.

Method Evaluation For measurement data inputs with various noise types and levels, the average EKF based parameter estimation results are tabulated in Table 1, and the recovered elasticity distributions are shown in Fig. 2.

Due to the coupling between the state variables and system parameters, the precision of the EKF estimate for the noise-free case has dropped from the LS result. For input data corrupted by Gaussian noises, however, EKF typically achieves much better results, even though the convergence speed is quite slow (Fig. 3). It is also well known that EKF could be greatly affected by the quality of the initializations. In order to investigate the effect of initial modulus values on the algorithm convergence, experiments have been conducted using $\hat{\theta}(0) = 95$, $\hat{\theta}(0) = 65$, and $\hat{\theta}(0) = 35$ for Gaussian data inputs. As shown in Fig. 4, a faster convergence is achieved when a proper initial value is chosen. However, the

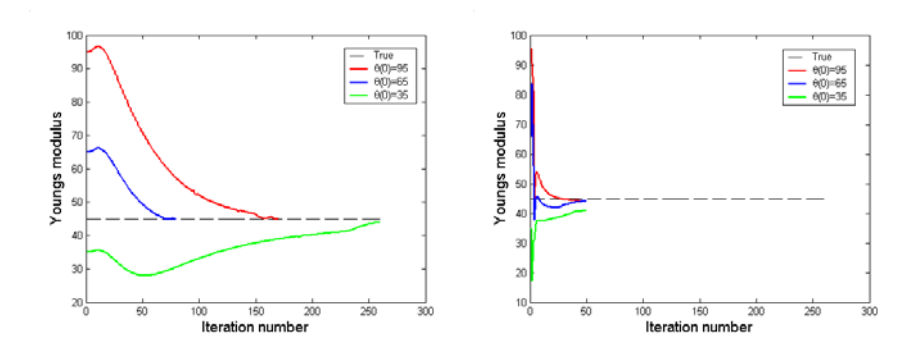


Fig. 4. Convergence sensitivity to different initial values (Gaussian inputs) for the EKF (left) and \mathcal{H}_{∞} -NPFSI (right) estimation of the soft region.

convergence rates from the upper side and the lower side of the initializations are not symmetric, which hinder the possibility to choose the *optimal* initial values in a symmetric fashion. Further, comparing the estimation results for Gaussian and Poisson inputs (Fig. 5), it is indicative that EKF is far from optimal for non-Gaussian noises and may be subject to divergence, at least during certain period of the iterative process, which motivates us to seek more robust strategies.

3.4 \mathcal{H}_{∞} Filters

Because of the deficiency of the LS and EKF methods to deal with noisy inputs, especially the non-Gaussian measurement data, we have developed two robust, mini-max parameter identification strategies based on the \mathcal{H}_{∞} filtering principles [3], which assume no specific types of noise distribution. While the full-state-derivative information (FSDI) method takes into account of the process noise v(t) and the initial parameter estimation error $\theta - \theta(\hat{0})$, the noise-perturbed full-state information (NPFSI) method also considers the measurement noise e(t) and the initial state estimation error $x - \hat{x}(0)$.

FSDI Method We introduce a cost function that measures the worst-case attenuation from the additive process disturbance as well as error in the initial estimate of θ to the estimation error over an interval of interest:

$$sup \frac{\|\theta - \hat{\theta}\|_{Q}^{2}}{\|v\|^{2} + |\theta - \theta(\hat{0})|_{Q_{0}}^{2}} < \gamma^{2}$$
(15)

where $\theta(0)$ is an a priori estimate of the parameter vector θ , $\| \bullet \|_Q^2$ is a L_2 seminorm with weighting function Q, $| \bullet |_{Q_0}^2$ is the Euclidean norm of $\bullet^T Q_0 \bullet$, and v is the process noise. Different from \mathcal{H}_2 (Kalman) filter based framework, the \mathcal{H}_{∞} method has many solutions corresponding to different γ values. Nevertheless,

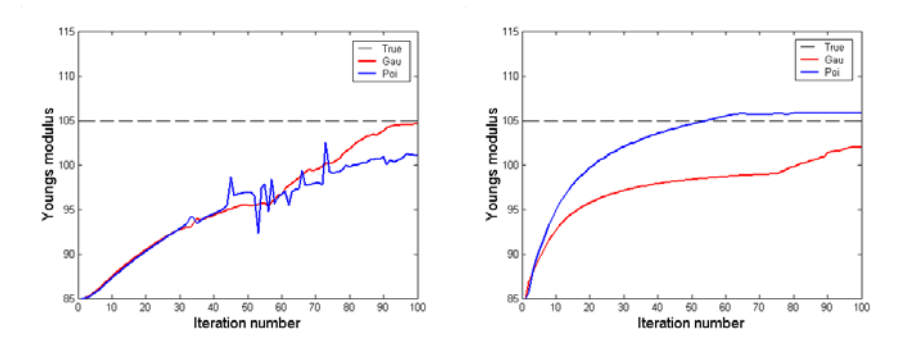


Fig. 5. Estimation sensitivity under different types (Gaussian and Poisson) of noises: EKF (left) and \mathcal{H}_{∞} -NPFSI (right) methods

if the optimal performance level γ^* does exist [3], the following solutions are optimal in mini-max sense for every $\gamma > \gamma^*$:

$$\dot{\hat{\theta}} = \Sigma^{-1} \mathcal{A}_c^T (\dot{x} - \mathcal{B})
\dot{\Sigma} = \mathcal{A}_c^T \mathcal{A}_c - \gamma^{-2} Q; \quad \Sigma(0) = Q_0$$
(16)

$$\dot{\Sigma} = \mathcal{A}_c^T \mathcal{A}_c - \gamma^{-2} Q; \quad \Sigma(0) = Q_0 \tag{17}$$

Hence, the \mathcal{H}_{∞} filter of FSDI form can be treated as a more general framework for material parameter estimation from clean kinematics measurement. If we let $\gamma \to \infty$, the limiting filter would converge to the aforementioned least-squares estimator. Let $Q = \mathcal{A}_c^T \mathcal{A}_c$, we have the following:

$$\gamma^* = 1, \dot{\hat{\theta}} = Q_0^{-1} \mathcal{A}_c^T (\dot{x} - \mathcal{B}) \tag{18}$$

which is the generalized least-mean-squares filter.

NPFSI Method In practice, inaccuracies are often due to unmodeled dynamics or measurement errors that are not considered when the model is built. To cope with such situations, we introduce a more complete cost function for all $\gamma > \gamma^*$:

$$sup \frac{\|\theta - \hat{\theta}\|_{Q}^{2}}{\|v\|^{2} + \|e\|^{2} + |\theta - \hat{\theta}(0)|_{Q_{0}}^{2} + |x - \hat{x}(0)|_{Q_{1}}^{2}} < \gamma^{2}$$
(19)

Here, $\hat{x}(0)$ is initial estimates for x(0), Q_1 is a weighting factor, and e models the measurement uncertainty. Under this criterion, we come to the solution:

$$\begin{bmatrix} \hat{x} \\ \hat{\theta} \end{bmatrix} = \begin{bmatrix} F \mathcal{A}_c(x) \\ 0 & 0 \end{bmatrix} \begin{bmatrix} \hat{x} \\ \hat{\theta} \end{bmatrix} + \begin{bmatrix} B_c w(t) \\ 0 \end{bmatrix} + \Sigma^{-1} H^T(y - \hat{x})$$
 (20)

$$\dot{\Sigma} = -\Sigma \begin{bmatrix} F \mathcal{A}_c(x) \\ 0 & 0 \end{bmatrix} - \begin{bmatrix} F^T & 0 \\ \mathcal{A}_c^T & 0 \end{bmatrix} \Sigma + \begin{bmatrix} I & 0 \\ 0 & -\gamma^2 Q \end{bmatrix} - \Sigma \begin{bmatrix} I & 0 \\ 0 & 0 \end{bmatrix} \Sigma$$
 (21)

In general, it is difficult to determine the optimal γ^* , and it may even be infinite which means that no guaranteed disturbance attenuation level can be achieved. In fact, however, if Q is chosen, γ^* can be obtained analytically. For a fixed γ , it is necessary to have $\Sigma>0$ for the existence of the identifier. Note that partitioning this matrix as $\Sigma=\begin{bmatrix} \Sigma_1 & \Sigma_2 \\ \Sigma_2^T & \Sigma_3 \end{bmatrix}$, the Schur test implies that $\Sigma>0$ if and only if $\dot{H}=\Sigma_2^T\Sigma_2-\gamma^2Q>0$, $\Pi(0)=Q_0$ and $\Sigma_1>0$. Hence, if $\Sigma_1(0)$ is chosen to be identity matrix and $Q=\Sigma_2^T\Sigma_2$, γ^* will be 1 [3].

Method Evaluation The two \mathcal{H}_{∞} methods are evaluated using the synthetic data and the convergence criteria are the same as the EKF one. $\gamma=3$ has been used in our experiments. The estimated Young's moduli are listed in Table 1 (both FSDI and NPFSI) and shown in Fig. 2 (NPFSI results only). As a generalized LS methods, the FSDI performs well for noise-free and low-noise inputs, but fails to converge for 20dB cases. While underperforming EKF estimator somewhat for Gaussian inputs, it is obvious that the \mathcal{H}_{∞} -NPFSI framework gives the best overall results when the data noises are not Gaussian. Further, even for Gaussian noises, NPFSI converges much faster than EKF, and it is not affected by the initial values of the Young's modulus (Fig. 4). In Fig. 3, the mean values with standard derivation of the estimates are plotted as a function of iterative numbers. It is evident that NPFSI results in faster and more stable convergence of the estimates for both Gaussian and Poisson inputs.

In a further sensitivity test of the algorithms to different types of noises, the convergence of the Young's modulus estimate for a particular element is given in Fig. 5, where the red and blue curves are generated for the SNR=30dB (Gaussian) and SNR=30dB (Poisson) input data respectively. It is clear that EKF has certain desirable optimality properties for Gaussian noisy inputs. However, the EKF results for Poisson noises are pretty bad, with unstable bursts during the convergence process. It seems that if the assumptions on the noise statistics are violated, it is possible that small noise errors may lead to large estimation errors for EKF. On the other hand, very stable convergence results are obtained using the NPFSI method for two sets of data contaminated by different types of noise, showing its desired robustness for real-world problems.

4 Applications and Discussion

4.1 Canine Imaging Data

The displacements of the canine heart wall are reconstructed using the active region model [13] on MR phase contrast images, which also provides the corresponding velocity information. The histological staining of the post mortem myocardium (Figure 7), with the infarct region highlighted, provides the clinical gold standard for the assessment of the image analysis results. Based on the reconstructed displacements and measured velocities (Fig. 6), the \mathcal{H}_{∞} -NPFSI and the EKF frameworks are used to recover the elasticity modulus distribution,

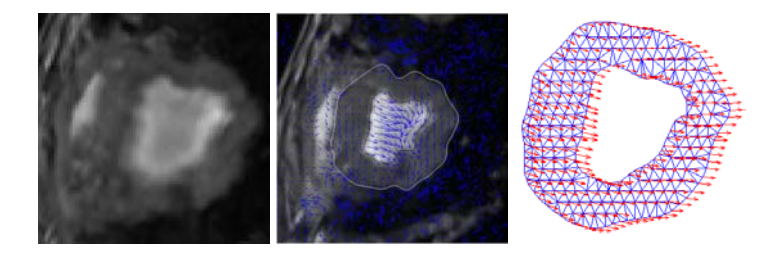


Fig. 6. A mid-ventricle MR image of a canine heart (left), velocity data (middle), and the displacement data acquired from the spatio-temporal active region method (right).

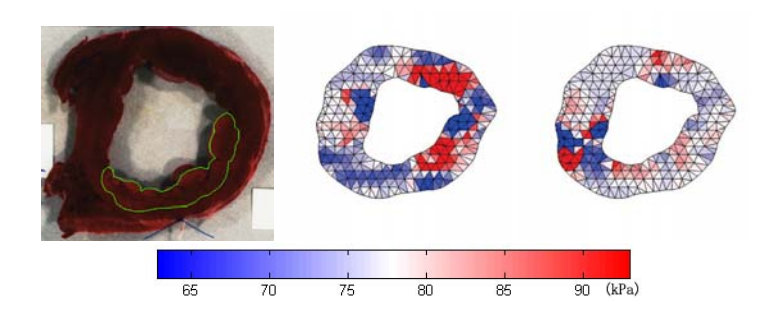


Fig. 7. TTC-stained post mortem left ventricular myocardium with infarcted zone highlighted (left), NPFSI (middle) and EKF (right) estimated Young's modulus maps.

where Poisson's ratio are fixed at 0.47 to model approximate incompressibility and the initial estimates of Young's modulus are set to be $75\mathrm{kPa}$.

4.2 Results and Discussion

The experimental results obtained with real canine imaging data are presented in Fig. 7, where the middle map depicts the NPFSI results and the right one for EKF results. It is observed that both the estimated Young's modulus distribution patterns agree pretty well with the highlighted histological staining results, i.e. the infarcted myocardium is harder than the normal tissue. As a continuation of this work, future study will be extended to time-varying estimation of the elasticity with more realistic material models.

References

- 1. Bathe, K.: Finite Element Procedures in Engineering Analysis. Prentice Hall (1982)
- Creswell, L.L., Moulton, M.J., Wyers, S.G., Pirolo, J.S. et al.: An Experimental Method for Evaluting Constitutive Models of Myocardium in vivo Hearts. American J. Physio. 267 (1994) H853–H853

- 3. Didinsky, G., Pan, Z., Basar, T.: Parameter Identification for Uncertain Plants using \mathcal{H}_{∞} Methods. Automatica. **31** (1995) 1227–1250
- Fung, Y.C.: A First Course in Continuum Mechanics: for Physical and Biological Engineers and Scientists. 3rd edn. Prentice Hall (1994)
- 5. Kallel, F., Bertrand, M.: Tissue Elasticity Reconstruction Using Linear Perturbation Method. IEEE Trans. Med. Imag. 15 (1996) 299–313
- Muthupilla, R., Lomas, D.J., Rossman, P.J., Greenleaf, J.F., Manduca, A., Ehman, R.L.: Magnetic Resonance Elastography by Direct Visualization of Propagating Acoustic Strain Waves. Science. 269 (1995) 1854-1857
- Raghavan, R.H., Yagle, A.: Forward and Inverse Problems in Imaging the Elasticity of Soft Tissue. IEEE Trans. Nucl. Sci. 41 (1994) 1639–1647
- 8. Shapo, B.M., Crowe, J.R., Skovoroda, A.R., et al.: Displacement and Strain Imaging of Coronary Arteries with Ultraluminal Ultrasound. IEEE Trans. Ultrason. Ferroelect. and Freg. Cont. 43 (1996) 234–246
- 9. Shi, P., Liu,H.: Stochastic Finite Element Framework for Simultaneous Estimation of Cadiac Kinematic Functions and Material Parameters. Medical Image Analysis 7 (2003) 445–464
- Skovoroda, A.R., Emelianov, S.Y., O'Donnel, M.: Tissue Elasticity Reconstruction Based on Ultrasonic Displacement and Strain Images. IEEE Trans. Ultrason. Ferroelect. and Freg. Cont. 42 (1995) 747–765
- 11. Tsap, L.V., Goldgof, D.B., Sarkar S.: Nonrigid Motion Analysis Based on Dynamic Refinement of Finite Element Models. IEEE. PAMI. **22** (2000) 526–543
- Weiss, H., Moore J.B.: Improved Extended Kalman Filter Design for Passive Tracking. IEEE Trans. Auto. Contr. 25 (1980) 807–811
- Wong, L.N., Liu, H., Sinusas, A.J., Shi, P.: Spatio-temporal Active Region Model for Simultaneous Segmentation and Motion Estimation of the heart. ICCV-VLSM03. Nice, France (2003) 193–200
- Zerhouni, E.A., Parish, D.M., Rogers, W.J., Yang, A., Shapiro, E.P.: Human Heart: Tagging with MR imaging - A Method for Noninvasive Assessment of Myocardial Motion. Radiology. 169 (1988) 59-63